

SaaFormer: Spectral-spatial Axial Aggregation Transformer for Hyperspectral Image Classification

Enzhe Zhao, Zhichang Guo, Yao Li, Dazhi Zhang

Abstract—Hyperspectral images (HSI) captured from earth observing satellites and aircraft is becoming increasingly important for applications in agriculture, environmental monitoring, mining, etc. Due to the limited available hyperspectral datasets, the pixel-wise random sampling is the most commonly used training-test dataset partition approach, which has significant overlap between samples in training and test datasets. Furthermore, our experimental observations indicates that regions with larger overlap often exhibit higher classification accuracy. Consequently, the pixel-wise random sampling approach poses a risk of data leakage. Thus, we propose a block-wise sampling method to minimize the potential for data leakage. Our experimental findings also confirm the presence of data leakage in models such as 2DCNN. Further, We propose a spectral-spatial axial aggregation transformer model, namely SaaFormer, to address the challenges associated with hyperspectral image classifier that considers HSI as long sequential three-dimensional images. The model comprises two primary components: axial aggregation attention and multi-level spectral-spatial extraction. The axial aggregation attention mechanism effectively exploits the continuity and correlation among spectral bands at each pixel position in hyperspectral images, while aggregating spatial dimension features. This enables SaaFormer to maintain high precision even under block-wise sampling. The multi-level spectral-spatial extraction structure is designed to capture the sensitivity of different material components to specific spectral bands, allowing the model to focus on a broader range of spectral details. The results on six publicly available datasets demonstrate that our model exhibits comparable performance when using random sampling, while significantly outperforming other methods when employing block-wise sampling partition.

Index Terms—Hyperspectral (HS) image classification, random sampling, long sequence information, block-wise sampling, Transformer.

I. INTRODUCTION

HYPERSPECTRAL remote sensing images are a type of satellite or airborne image that captures data across a wide range of wavelengths. Unlike traditional remote sensing images that capture data across just a few wavelengths (e.g., red, green, and blue), hyperspectral images capture data across hundreds of narrow spectral bands. Compared with other types of remote sensing images. This allows for a more detailed and precise analysis of the surface of the earth, as different materials and surfaces reflect light differently across the electromagnetic spectrum [1]. Therefore, HSI has been applied in various fields, such as astronomy, agriculture, and mineralogy. Consequently, HSI classification has emerged as

a highly active research area within the field of hyperspectral research. In the context of a high spectral image classification system, a typical sequential workflow encompasses the following stages: image restoration, encompassing tasks like denoising and missing data recovery [2], [3], dimensionality reduction [4], spectral unmixing [5]–[8], and feature extraction [9], [10]. These stages are executed in a consecutive manner, forming the overall processing pipeline.

During the early stages of hyperspectral image analysis, researchers explored and applied existing classification techniques from the fields of remote sensing and image processing. The Maximum Likelihood Classifier (MLC) [11], [12] and the Spectral Angle Mapper (SAM) [13] were among the earliest methods used for hyperspectral image classification. MLC assumes that pixel spectra in each class follow a specific probability distribution, typically a multivariate Gaussian distribution. However, this assumption may not hold true for complex hyperspectral data, leading to reduced classification accuracy. SAM is a geometric method for hyperspectral image classification that measures spectral similarity by calculating the angle between pixel spectra and reference spectra. However, it heavily relies on spectral angles and disregards spectral variations caused by factors such as illumination changes or surface conditions, greatly limiting its capability to accurately classify similar spectra. Furthermore, these methods may be affected by the curse of dimensionality, especially when the number of training samples is limited compared to the number of spectral bands. Feature extraction and selection play a vital role in reducing dimensionality and capturing pertinent information, leveraging technological advancements and enhanced computational capabilities. Researchers have developed techniques such as Principal Component Analysis, Linear Discriminant Analysis, and Wavelet Transform to address the challenges posed by the curse of dimensionality. However, these methods are often sensitive to outliers leading to misleading representations of the data. Support Vector Machines [15], [16] and Random Forests [17], [18], to better handle the complexity and high dimensionality of HSI. However, they primarily focus on pixel-based classification without considering spatial information. Hyperspectral images often contain valuable spatial and contextual information, and disregarding the spatial relationships among neighboring pixels may result in suboptimal outcomes.

Inspired by the great success of deep learning [19], which is capable of finding out intrinsic and potentially valuable knowledge from the vast amounts of pluralistic data [20], convolutional neural network (CNN) has emerged as a popular technique for hyperspectral image classification due to their ability

Corresponding author: Yao Li (E-mail: yaoli0508@hit.edu.cn)

Enzhe Zhao, Zhichang Guo, Yao Li and Dazhi Zhang are with the Department of Computational Mathematics, School of Mathematics, Harbin Institute of Technology, Harbin 150001, China.

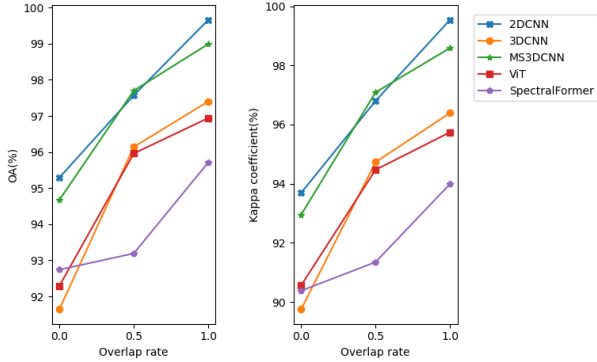


Fig. 1: Comparison of the accuracy of the overlap rate of training samples and test samples for different models.

to automatically learn hierarchical feature representations from the spectral bands of the input data. Taking into account the fact that hyperspectral data is comprised of a multitude of successive and interconnected spectral bands, Hu et al. [22] proposed 1DCNN Classifier to capture and assimilate localized dependencies that arise between adjacent spectral bands, thus enriching the overall understanding and interpretation of HSI. Concurrently, Mou et al. [23] effectively leverage the temporal aspect, treating it as a time series, and employ RNN framework as a viable approach to model the inherent dependencies and extract intricate spectral information. According to [24], [25], spatial context information plays an important role in the classification of HSI. 2DCNN has been introduced into this domain, due to the powerful feature extraction capabilities and its ability to effectively capture spatial correlations by employing convolutional operations and weight sharing to recognize feature distribution patterns in space. Yue et al. [27] proposed DCNNs-LR classifier, which generated spectral feature maps by performing outer products between different segments of the pixel’s spectra and stacked it with spatial feature maps consisting of dominant PCA bands of image patch around the pixel to form spatial-spectral input. Hyperspectral image can be conceptualized as a three-dimensional voxel data, thus presenting an opportunity to leverage the combined spectral and spatial knowledge through 3DCNN modeling. Furthermore, compared to 2DCNN, 3DCNN possess the characteristic of scale invariance, enabling it to effectively handle HSI of varying resolutions and sizes. Chen et al. [29] proposed a 3-D CNN-based FE model to semantically extract spatial-spectral features by considering local contextual information of HS images, achieving higher classification accuracies. Li et al [30] proposed 3DCNN-Based HSI Classification which views the HSI cube data altogether without relying on any preprocessing or post-processing, extracting the deep spectral-spatial combined features effectively. He et al [31] proposed M3D-DCNN model for HSI classification, which the joint modeling of multiple spectral bands can be achieved, allowing for the integration and fusion of diverse features across different scales.

As the mainstream backbone architecture, they have shown their powerful ability in extracting spatially structural infor-

mation and locally contextual information from HSI. Nevertheless, they can hardly be capable of capturing the sequence attributes well, particularly middle- and longterm dependencies. This unavoidably meets the performance bottleneck in the HSI classification task, especially when the classified categories are of a great variety and extremely similar in spectral signatures. Very recently, the vision transformer(ViT) [32] achieved the state-of-the-art effects on various vision domain tasks, providing new insight, inspiration, and creative space on vision related tasks. The introduction of Transformer effectively integrates spatial and spectral information through the self-attention mechanism and enhances the classification model’s understanding of comprehensive features. Moreover, the self-attention mechanism enables each position (or spectral band) to interact with all other positions, facilitating adaptive learning of feature relationships. Hong et al. [33] proposed SpectralFormer, which is capable of learning spectrally local sequence information from neighboring bands of HSI, yielding groupwise spectral embeddings. However, this partitioning approach may disrupt the continuity of spectral information, potentially impacting the classification accuracy of the model. Furthermore, the augmented computational costs and escalated memory demands are inevitable consequences arising from the inherent high-dimensional characteristics and expanding data size of HSI.

Hence, taking into account the inherent long sequential nature of HSI, we put forward a spectral-spatial axial aggregation transformer model named SaaFormer, which aims to perform feature extraction and fusion across multiple scales along the spectral dimension. This approach allows the model to effectively attend to both the global information and the fine-grained spectral details, thereby facilitating the extraction of more comprehensive and richer feature representations from HSI. And we used axial aggregation attention which not only allows efficient computation, but recovers large receptive field in stand-alone attention models, that makes our model having better generalization ability.

The main contributions of this paper can be summarized as follows:

1) We propose a spectral-spatial axial aggregation transformer framework for HSI classification problem, which performs multi-scale feature extraction and fusion on the input data while utilizing spectral shift operations to ensure information aggregation and feature extraction across different spectral components.

2) We propose a new block-wise dataset partition approach to avoid data leakage problem while maintaining nonlocal training samples. We re-evaluate the classification performance of state-of-the-art backbone networks on representative HS datasets;

3) We qualitatively and quantitatively evaluate the classification performance of the proposed model on the six public datasets of Indian Pines, Pavia University(PaviaU), Pavia Centre(Pavia), Salinas scene, Kennedy Space Center(KSC) and Botswana with extensive ablation studies. The experimental results demonstrate a significant superiority over classic transformer and other state-of-the-art backbone networks.

The remaining of the paper is organized as follows. Section

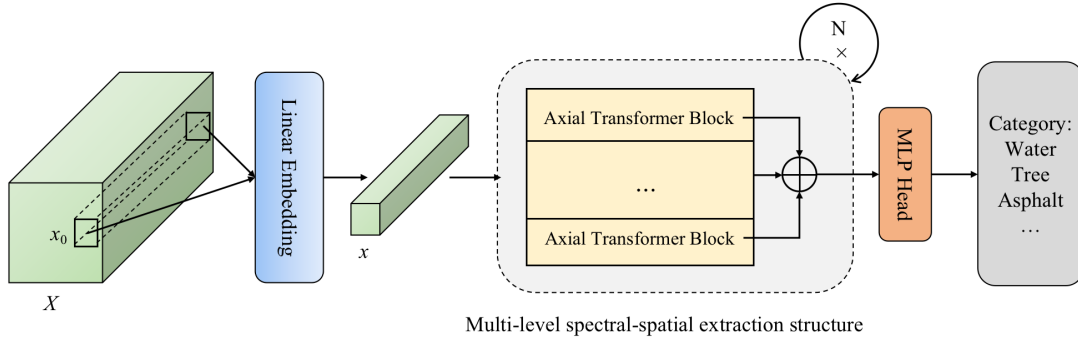


Fig. 2: Overview illustration of SaaFormer for HSI classification task.

II proposes a new evaluation method to alleviate the problem of data leakage, then we introduces the overall framework of the proposed SaaFormer and the detailed structure of each component. Otherwise, extensive experiments are conducted with ablation studies and discussions. Section IV draws comprehensive conclusions.

II. METHODOLOGY

A. Block-wise Sampling

Due to difficulties in collection and costs associated with the analysis of material's chemical and physical properties, ground truth data is very scarce in HSI datasets. For exploiting the spatial correlation, current paradigm commonly employs pixel-wise random sampling to divide the datasets, where each sample consists of a central pixel and its surrounding region. However, this sampling approach results in a high overlap between adjacent samples, leading to a significant similarity between the training and test sets and posing a risk of data leakage. An experiment was conducted wherein the test set was partitioned according to the extent of overlap with the samples in the training set to validate this hypothesis. As can be seen from Figure 1, we divide the test set into some parts according to the overlap rate, that is, the overlap rate is higher than 50%, the overlap rate is between 0%-50% and no overlap at all, and observe the change of accuracy on several different models. The experimental results indicated that test regions with higher overlap often exhibited higher accuracy. Therefore, this random sampling approach is prone to data leakage issues.

Therefore, we proposed an innovative block-wise sampling approach, as illustrated in Fig. 3, the hyperspectral dataset is divided into non-overlapping blocks of equal size, followed by the insertion of gaps to create distinct training and test sets. This partitioning method effectively addresses the issue of data leakage and enables more accurate performance evaluation of the model. By avoiding overlapping regions, we ensure the independence between the training and test sets, thereby mitigating the risk of information leakage. This novel block-wise sampling technique provides a more reliable and precise approach for analyzing HSI.

Taking into account each pixel of HSI represents the spectral curve of the substance here, which contains the sequence properties of spectral characteristics. This inspired us to adopt Transformer-based framework from a sequential perspective.

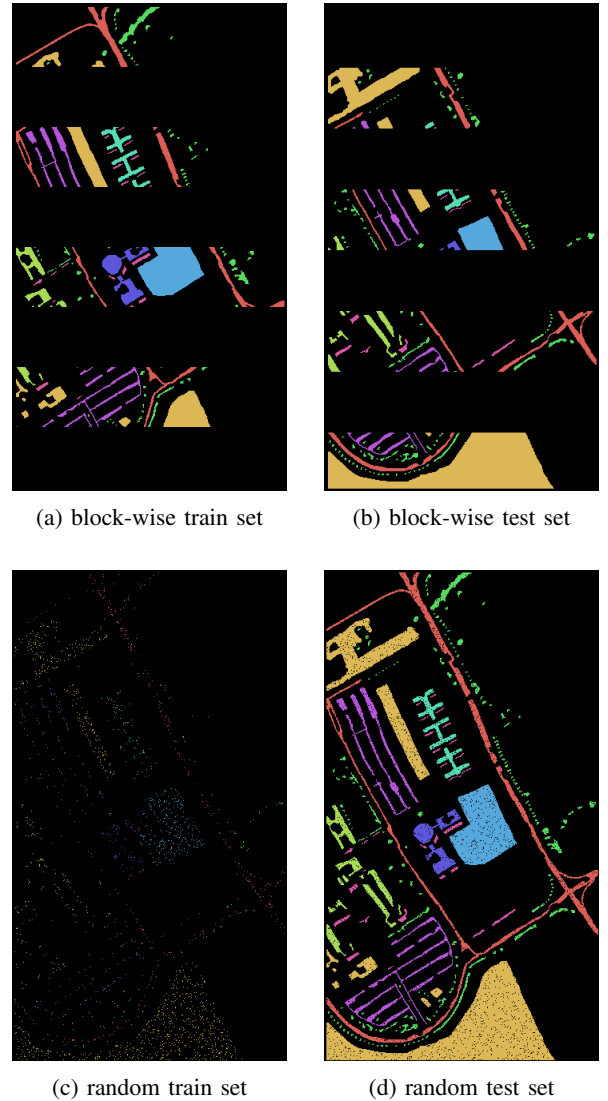


Fig. 3: Comparison diagram of PaviaU dataset by block-wise sampling and random sampling

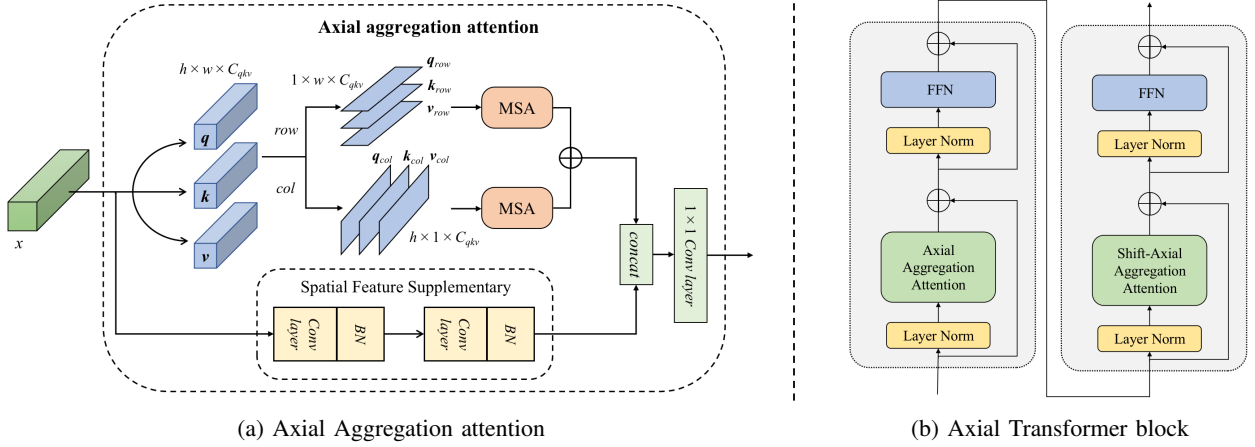


Fig. 4: Diagram of the Axial Transformer Block in the proposed SaaFormer.

The proposed SaaFormer exhibits enhanced generalization capability.

B. Overview of SaaFormer

We put forward a multi-level axial transformer model, named SaaFormer, which aims to perform feature extraction and fusion across multiple scales along the spectral dimension. Fig. 2 illustrates an overview of SaaFormer, which comprises two primary components: axial transformer block and multi-level spectral extraction. Given a HS image (i.e. a hyperspectral dataset) $X \in \mathbb{R}^{H \times W \times C}$, $x_0 \in \mathbb{R}^{h \times w \times C}$ represents one of the samples, the input sample x_0 undergo dimensionality transformation through linear embedding layer, followed by a multi-level spectral feature partitioning process. And the resulting feature maps of different scales are individually fed into axial transformer modules for feature extraction, enabling the extraction of relevant features at various spatial and spectral levels. These features are then fused to incorporate information from different scales. Finally, the fused features are input to the classification head to generate the output results. A detailed introduction of each structure will be carried out in the next subsection.

C. Axial Transformer Block

While the self-attention mechanism has showcased impressive performance across a range of tasks, its limitation of increased parameter and computational complexity cannot be disregarded, particularly when dealing with lengthy sequential data. Presently, there exist numerous lightweight modifications being explored to improve the self-attention mechanism [34]–[39], with the axial attention mechanism standing out as a promising candidate in various tasks [40]–[43]. Hence, in addressing the challenge of HSI classification, we incorporate the squeeze-enhanced axial attention mechanism [43]. However, due to its imperfect alignment with the specific characteristics of high-dimensional spectral data, we have undertaken further improvements by designing the spatial-spectral axial aggregation attention mechanism.

Our proposed SaaFormer uses an improved spectral-spatial axial attention mechanism for feature extraction which can

adaptively attend to different spectral channels. And by considering the interrelationships among spectral bands at each pixel location and aggregating features in the spatial domain, it enables the extraction of meaningful context and relevance in HSI. In contrast to conventional attention mechanisms, its efficiency enables us to build models to learn long range continuous spectral curve characteristics. Moreover, through the filtration of irrelevant information in input samples, it enhances the utilization efficiency of crucial features. Consequently, it reduces the model’s sensitivity to noise and interference, ultimately enhancing its generalization capability.

Firstly, $\mathbf{q} = W_q \mathbf{x}$, $\mathbf{k} = W_k \mathbf{x}$, and $\mathbf{v} = W_v \mathbf{x}$ are all linear projections of the input feature map $\mathbf{x} \in \mathbb{R}^{h \times w \times c}$ where $W_q, W_k, W_v \in \mathbb{R}^{C_{qkv} \times c}$ are all learnable matrices. Then, we achieve horizontal extrusion by taking the maximum value of the query feature map in the width direction. In the same way, we get the vertical squeeze on the vertical direction. i.e. $\mathbf{q}_{row} = \max_w(\mathbf{q})$, $\mathbf{q}_{col} = \max_h(\mathbf{q})$. The aggregation operation on \mathbf{q} also repeats on \mathbf{k} and \mathbf{v} , so we finally get $\mathbf{q}_{row}, \mathbf{k}_{row}, \mathbf{v}_{row} \in \mathbb{R}^{h \times 1 \times C_{qkv}}$, $\mathbf{q}_{col}, \mathbf{k}_{col}, \mathbf{v}_{col} \in \mathbb{R}^{1 \times w \times C_{qkv}}$.

The aggregation operation in the proposed approach consolidates global information by compressing it into a single axis, as demonstrated by Equation 1. By condensing the global information into a single axis, the aggregation operation enables more efficient and effective extraction of global semantic features.

$$\mathbf{h}_{(i,j)} = \sum_{p=1}^h \text{softmax}_p \left(\mathbf{q}_{(h)i}^\top \mathbf{k}_{(h)p} \right) \mathbf{v}_{(h)p} + \sum_{p=1}^w \text{softmax}_p \left(\mathbf{q}_{(v)j}^\top \mathbf{k}_{(v)p} \right) \mathbf{v}_{(v)p} \quad (1)$$

It is worth mentioning that the spatial-spectral axial aggregation attention mechanism lacks explicit position information, which limits its ability to effectively utilize sequential context. To address this limitation, we follow [35], [41], [43], [44] by including a relative position bias to each head. And apply the learnable relative position coding directly to query, key, value. By incorporating learnable relative position embed-

dings, denoted as $\mathbf{r}_{row}^q, \mathbf{r}_{row}^k, \mathbf{r}_{row}^v \in \mathbb{R}^{h \times 1 \times C_{qkv}}$, we enable the attention mechanism to be aware of the positional relationships in the input feature map. This augmentation allows the aggregation attention module to leverage the positional cues and enhance its capability to capture sequential information effectively. Perform the same operation in the vertical direction to get $\mathbf{r}_{col}^q, \mathbf{r}_{col}^k, \mathbf{r}_{col}^v \in \mathbb{R}^{1 \times w \times C_{qkv}}$. Thus, the positional-aware aggregation attention can be expressed as Equation 2.

$$\begin{aligned} \mathbf{h}_{(i,j)} = & \sum_{p=1}^h \text{softmax}_p \left(\left(\mathbf{q}_{(row)i} + \mathbf{r}_{(row)i}^q \right)^\top \left(\mathbf{k}_{(row)p} \right. \right. \\ & \left. \left. + \mathbf{r}_{(row)p}^k \right) \right) \left(\mathbf{v}_{(row)p} + \mathbf{r}_{(row)p}^v \right) \\ & + \sum_{p=1}^w \text{softmax}_p \left(\left(\mathbf{q}_{(col)j} + \mathbf{r}_{(col)j}^q \right)^\top \left(\mathbf{k}_{(col)p} \right. \right. \\ & \left. \left. + \mathbf{r}_{(col)p}^k \right) \right) \left(\mathbf{v}_{(col)p} + \mathbf{r}_{(col)p}^v \right) \end{aligned} \quad (2)$$

As is shown in the upper path of Fig. 4a, the attention compresses the feature map to a vertical or horizontal axis and compute self-attention over a single axis at a time, then, add a horizontal and a vertical axial attention module to obtain the global receptive field. Its efficiency enables us to attend over large regions and build models to learn long range or even global interactions. Otherwise, neighboring pixels are highly interdependent because most of the land covers are much bigger than the size of the pixel. It has been prevalent to utilize spatial information along with spectral data during analysis to combat the problem of high dimensionality. Therefore, our model integrates spatial constraint information while considering the characteristics of spectral sequences making it well-applicable to the highly accurate and fine classification.

The axial attention mechanism will pay more attention to the important spectral characteristics of the sample space and extract global spectral curve efficiently which may sacrifice the spatial local details. Hence, we apply an auxiliary spatial feature extraction module which is made up of 3×3 convolution and batch normalization to supplementary the spatial details and maintain the spatial structure of the sample. As is shown in the down path of Fig. 4a, by using convolution layers, auxiliary spatical local details can be aggregated. Finally, the enhancement feature will be fused with the feature given by aggregation attention.

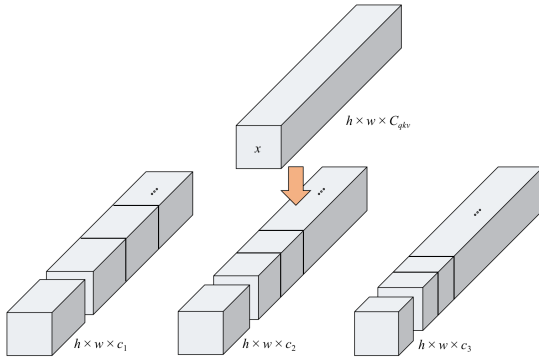


Fig. 5: Diagram of the Multi-level Spectral-spatial Extraction Structure.

D. Multi-level Spectral-spatial Extraction

Multi-scale feature extraction has demonstrated significant benefits in image processing, as it enables models to capture information at various levels and granularities by extracting features, thereby enhancing their robustness. [46]. Meanwhile, in view of the diverse absorption or reflection characteristics of different materials for different wavelengths of light, as well as the potential presence of noise interference in obtained spectral curves, we propose a hierarchical feature extraction structure. It divides the input samples into non-overlapping continuous spectral segments of varying lengths, which are considered as spectral partition, as illustrated in Fig 5, the feature map $x \in \mathbb{R}^{h \times w \times C_{qkv}}$ is divided into spectral partitions of different lengths (i.e. c_1, c_2, c_3) in spectral dimensions, an axial transformer blocks is performed within each spectral partition, followed by feature fusion. This approach reduces redundancy in HSI and enables better utilization of spectral information, thereby enhancing the model's perception of different material components and its capability to capture spectral details.

However, this approach has certain limitations as the connections across different partitions is restricted. To introduce cross spectral partitions connections while maintaining the efficient computation of non-overlapping partitions, we propose a shifted spectral partition operation, as illustrated in Fig 6. Specifically, after an initial feature extraction step, we perform a subsequent re-aggregation of information between different segments in the spectral dimension, followed by another round of feature extraction. The first block uses a regular spectral partitioning strategy to get $x_1, x_2 \in \mathbb{R}^{h \times w \times c_1}$. Then, x_1 is divided into part A and part B, and x_2 is divided into part C and part D where $A, B, C, D \in \mathbb{R}^{h \times w \times \frac{c_1}{2}}$. The part B and part C are formed into new x'_1 . This operation enhances the capacity to capture fine-grained spectral details and exploit the interdependencies among different spectral partitions, thereby effectively leveraging the abundant spectral information inherent.

Due to the continuity of spectral curves in HS images, the spectral shift operation aggregates the first and last spectral segments. However, from a physical perspective, the first and last segments are completely unrelated and represent distinct spectral features. To prevent erroneous feature extraction and misclassification, we apply a masking process to the irrelevant aggregated spectral segments, considering them as invalid information. This prevents the model from erroneously utilizing these segments. Through this masking operation, we preserve meaningful spectral features and ensure accurate classification and recognition of relevant features.

With the shifted spectral partitioning approach, the specific flowchart is shown in Fig. 4a and consecutive Axial attention blocks are computed as

$$\begin{aligned} \hat{f}^l &= \text{AxialAtten} \left(\text{LN} \left(f^{l-1} \right) \right) + f^{l-1} \\ f^l &= \text{FFN} \left(\text{LN} \left(\hat{f}^l \right) \right) + \hat{f}^l \\ \hat{f}^{l+1} &= \text{SAxialAtten} \left(\text{LN} \left(f^l \right) \right) + f^l \\ f^{l+1} &= \text{FFN} \left(\text{LN} \left(\hat{f}^{l+1} \right) \right) + \hat{f}^{l+1} \end{aligned} \quad (3)$$

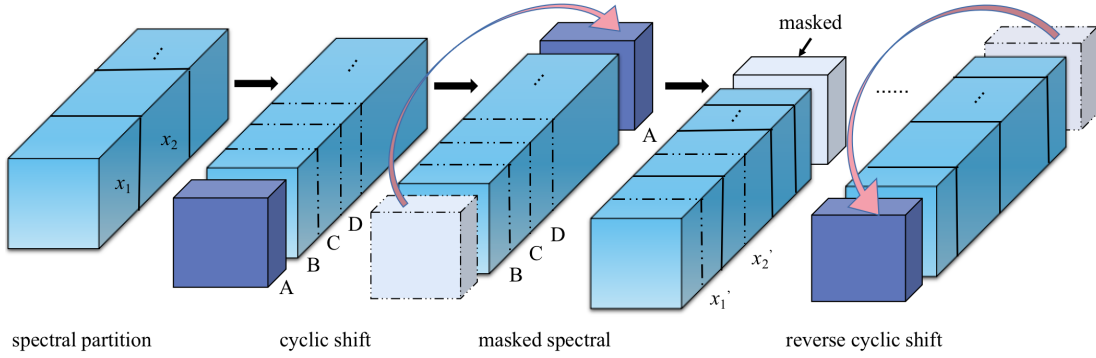


Fig. 6: Diagram of the shifted spectral partitioning structure.

III. EXPERIMENTS

In this part, we first introduce several well-known HSI datasets, and give the datasets division method we proposed. Then compare SaaFormer with other state-of-the-art methods in the new division method. Finally, extensive experiments are conducted with ablation analysis to assess the HSI classification performance of the proposed model.

A. Data Description

Experiments are conducted on six hyperspectral datasets¹. The detailed descriptions of these datasets are listed as follows.

- The Indian Pines dataset was collected by the airborne visible/infrared imaging spectrometer sensor (AVIRIS) over the Indian Pines test site in June 1992. It consists of 145×145 pixels and has 220 spectral bands. The dataset has 20 m per pixel spatial resolutions and 10 nm spectral resolutions covering a spectrum range of 200–2400 nm. In the experiment, after removing 20 noisy and water absorption bands, 200 spectral bands are retained, i.e., 1–103, 109–149, and 164–219. The ground truth is composed of 16 vegetation classes.
- The Pavia Centre and Pavia University dataset are acquired by the ROSIS sensor during a flight campaign over Pavia, northern Italy. The number of spectral bands is 102 for Pavia Centre and 103 for Pavia University. Pavia Centre is a 1096×1096 pixels image, and Pavia University is 610×610 pixels, but some of the samples in both images contain no information and have to be discarded before the analysis. The geometric resolution is 1.3 meters. Both image groundtruths differentiate 9 classes each.
- The Salinas scene dataset was collected by the 224-band AVIRIS sensor over Salinas Valley, California, and is characterized by high spatial resolution (3.7-meter pixels). The area covered comprises 512 lines by 217 samples. As with Indian Pines scene, this dataset discarded the 20 water absorption bands, in this case bands: [108–112], [154–167], 224. This image was available only as at-sensor radiance data.

- The Kennedy Space Center (KSC) dataset was acquired by the NASA AVIRIS (Airborne Visible/Infrared Imaging Spectrometer) instrument over the Kennedy Space Center, Florida, on March 23, 1996. AVIRIS acquires data in 224 bands of 10 nm width with center wavelengths from 400–2500 nm. The KSC data, acquired from an altitude of approximately 20 km, have a spatial resolution of 18 m. After removing water absorption and low SNR bands, 176 bands were used for the analysis. For classification purposes, 13 classes representing the various land cover types that occur in this environment were defined for the site.
- The Botswana dataset was acquired by the NASA EO-1 satellite over the Okavango Delta, Botswana in 2001–2004. The Hyperion sensor on EO-1 acquires data at 30 m pixel resolution over a 7.7 km strip in 242 bands covering the 400–2500 nm portion of the spectrum in 10 nm windows. Uncalibrated and noisy bands that cover water absorption features were removed, and the remaining 145 bands were included as candidate features: [10–55, 82–97, 102–119, 134–164, 187–220]. The data analyzed in this study, acquired May 31, 2001, consist of observations from 14 identified classes representing the land cover types in seasonal swamps, occasional swamps, and drier woodlands located in the distal portion of the Delta.

B. Data Division

1) *Random Sampling*: The method of random sampling in hyperspectral datasets refers to treating each valid pixel along with its surrounding rectangular window of the same size (e.g. 5×5) as a sample within a complete hyperspectral image. Subsequently, all samples are randomly divided into train and test sets based on a predetermined ratio. This identical training and testing set division ratio is applied to all six hyperspectral datasets. 5% samples from each class are randomly selected as the training set, and the remaining samples are used for test.

2) *Block-wise Sampling*: Block sampling method refers to dividing a complete hyperspectral dataset into non-overlapping areas according to a certain size, and each area is divided into a training set or test set as a collation. In our experiment, We employ a gapped-block method to partition the training set and the test set, select a smaller sample area as the training set, and use the rest as the test set. The selection

¹All these datasets can be obtained at https://www.ehu.es/ccwintco/index.php/Hyperspectral_Remote_Sensing_Scenes

of segmented size is to make each class of sample exist in the minimum value of the training set and test set.

C. Experimental Setting

1) Evaluation Metrics: We evaluate the classification performance of each model quantitatively in terms of three commonly used indices, i.e., OA, AA, and κ . Here, OA represents the number of correctly classified samples out of the total test samples; AA represents the average of class-wise classification accuracies; and Kappa is a metric of statistical measurement which provides mutual information regarding a strong agreement between the ground truth map and classification map. Expressed by formula as

$$OA = \frac{1}{N} \sum_{i=1}^{row} x_{ii}$$

$$AA = \frac{1}{N} \sum_{i=1}^N \frac{x_{ii}}{x_{i+}}$$

$$Kappa = \frac{N \sum_{i=1}^{row} x_{ii} - \sum_{i=1}^{row} (x_{i+} \times x_{+i})}{N^2 - \sum_{i=1}^{row} (x_{i+} \times x_{+i})}$$

where N is the total number of categories, and x_{ij} indicates that the real category is i , which is predicted to be the number of samples in category j . And r represents the number of samples correctly classified in each category, x_{i+} is the total number of samples in that category in the predicted sample, and x_{+i} is the total number of samples in that category in the label.

2) Comparison With State-of-the-Art Backbone Networks: In order to verify the classification performance of the proposed SaaFormer, five representative methods based on convolutional neural network and recurrent neural network for HSI classification, 1DCNN Classifier [22], 2DCNN-LR [29], 3-DCNN-based FE model [30], M3D-DCNN [31], RNN [23] and two models based on Transformer, the classical ViT [32] and SpectralFormer [33] are used as the comparison methods. The parameter configurations of these compared methods are detailed as follows.

- For the 1DCNN Classifier, as suggested by the literature [22], one convolutional block is defined as the basic network unit, including a set of 1D convolutional filters with the output size of 20, a maxpooling layer, and a hyperbolic tangent function tanh as the activation function. Two fully connected layers are finally added on the top of the 1DCNN.
- For 2DCNN-LR, which has three 2D convolutional blocks and a softmax layer. Each convolutional block of 2D CNN consists of a 2D convolutional layer, a BN layer, a max-pooling layer, and a ReLU activation function.
- For 3-DCNN-based FE model, the spatial window size of 3D input and the parameters of the 3D convolution kernel is set to the default value in [30].
- For M3D-DCNN, as suggested by literature [31], uses 3D convolution kernel of different sizes ($1 \times 1 \times 1, 3 \times 1 \times 1, 5 \times 1 \times 1, 11 \times 1 \times 1$) for multi-scale feature extraction at the same time, and then adds the extracted features.

- For RNN framework, followed by [23], there are two recurrent layers with the gated recurrent unit (GRU). Each of them has 128 neuron units.
- For the Transformer model, we follow the ViT network architecture [32], i.e., The original self-attention mechanism is used for feature extraction for input. In detail, four encoder blocks with eight attention heads are used in the ViT-based network for HSI classification.
- For SpectralFormer, the input size and the hyperparameters are set to the default value in [33]
- For SaaFormer, the embedded spectrum with 128 units is fed into two cascaded transformer encoder blocks for HS image classification. Each encoder block consists of a four-head axial aggregation attention layer, an MLP, and a GELU nonlinear activation layer. The dropout layer is employed after encoding positional embeddings and in MLPs for inhibiting 10% neurons. the patch size is empirically set as 5×5 .

3) Implementation Details: Our proposed model was implemented on the PyTorch platform using a workstation with i7-6850K CPU, 128-GB RAM, and an NVIDIA GTX 3090Ti 11-GB GPU. We adopt the Adam optimizer [45] with a minibatch size of 64. The learning rate is initialized with $5e-4$ and decayed by multiplying a factor of 0.9 after each one-tenth of total epochs. We roughly set the epochs on the two datasets to 200.

D. Quantitative Results and Analysis of HSI Classification Models

To verify the classification performance of the proposed model, experiments are executed on aforementioned datasets which are set to be compared by block division and random division respectively. The OA, AA, and kappa of classification results are used as evaluating indicators under different training set and test set.

As shown in Fig.7, three statistical graphs illustrate the comparative results of different datasets using block-wise sampling and random sampling methods. The dashed lines represent the accuracy of our proposed model under block-wise sampling and random sampling. From the graph, it can be observed that the light-colored bars of each model are higher than the dark-colored bars, indicating the potential risk of data leakage when using random sampling. Particularly, the 2DCNN model exhibits significant differences, indicating overfitting issues and poor generalization capability. In contrast, SaaFormer shows smaller variances and achieves the highest accuracy under block-wise sampling among all the six tested datasets, demonstrating its excellent generalization capability. Moreover, SaaFormer achieves the best performance under random sampling method on Botswana, KSC, IndianPines, and Salinas datasets. On PaviaU and PaviaC, the 2DCNN model has higher accuracy than SaaFormer which is caused of serious overfitting.

Table I and Table II provide detailed data on the three evaluation metrics obtained using different partitioning methods on the PaviaU and Botswana datasets. The bold numbers indicate the best accuracy achieved. It is evident that our

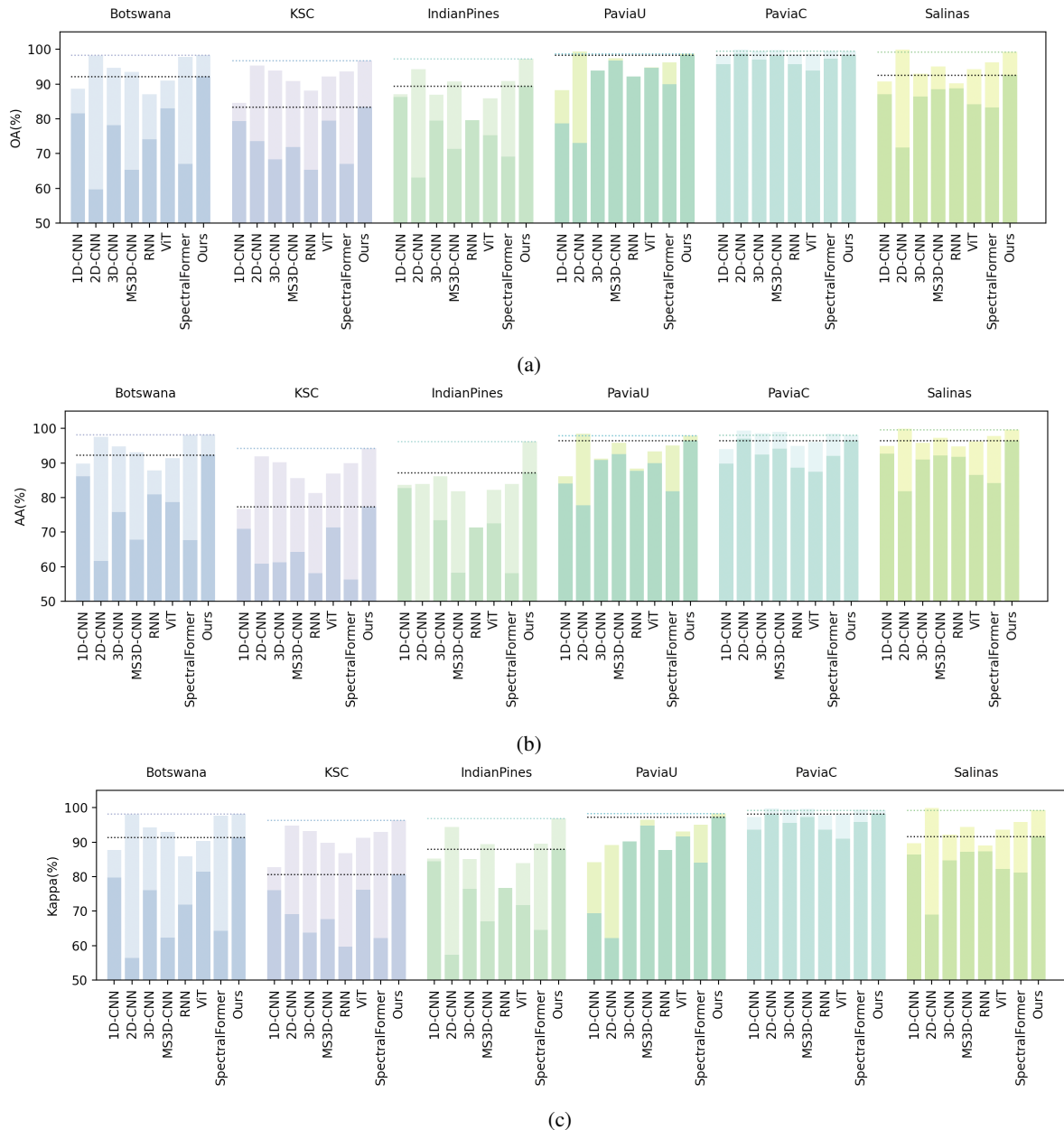


Fig. 7: Comparison of the results of different models on the three indicators of OA, AA and Kappa on the six datasets. The lighter-colored bars represent classification metrics of random sampling method. The darker-colored bars represent metrics of block-wise sampling method.

proposed model achieves the best accuracy in almost all cases. Furthermore, it is encouraging to note that the variations in the three evaluation metrics across different partitioning methods are minimal, even within a range of 1%. This indicates that our model not only maintains high accuracy across different datasets but also exhibits consistent performance under different partitioning methods. This demonstrates the excellent generalization capability and robustness of the proposed SaaFormer.

E. Ablation Study

We investigate the performance gain of the proposed SaaFormer in terms of classification accuracies by apply-

ing different structures (i.e. Multi-level Spectral Extraction). For that, we conduct extensive ablation experiments on the six datasets to verify the effectiveness of the structure in SaaFormer for HSI classification applications, as listed in Table III.

The experimental results from Table III demonstrate that the introduction of the multi-level spectral extraction structure consistently leads to higher accuracy in our model across different datasets (beyond around 3% OAs on the Salinas dataset), independent of the data partitioning schemes. This finding highlights the effectiveness of the multi-level spectral extraction structure in capturing underlying patterns and correlations within the spectral curves, enabling the model to

TABLE I: Comparison of classification accuracy of random sampling and block division on PaviaU dataset

	OA		AA		Kappa	
	Random	Block	Random	Block	Random	Block
1DCNN	0.8820	0.7868	0.8619	0.8405	0.8416	0.6934
2DCNN	0.9935	0.7307	0.9847	0.7774	0.8914	0.6216
3DCNN	0.9121	0.9391	0.9130	0.9086	0.8825	0.9026
MS3DCNN	0.9736	0.9673	0.9580	0.9261	0.9651	0.9477
RNN	0.9057	0.9223	0.8833	0.8774	0.8743	0.8767
ViT	0.9480	0.9462	0.9331	0.8993	0.9312	0.9160
SpectralFormer	0.9625	0.8992	0.9499	0.8188	0.9503	0.8405
SaaFormer	0.9875	0.9828	0.9795	0.9649	0.9833	0.9726

TABLE II: Comparison of classification accuracy of random sampling and block-wise sampling on Botswana dataset

	OA		AA		Kappa	
	Random	Block	Random	Block	Random	Block
1DCNN	0.8869	0.8151	0.8977	0.8611	0.8775	0.7973
2DCNN	0.9818	0.5968	0.9757	0.6169	0.9803	0.5645
3DCNN	0.9465	0.7810	0.9475	0.7585	0.9420	0.7609
MS3DCNN	0.9345	0.6529	0.9306	0.6786	0.9290	0.6233
RNN	0.8700	0.7406	0.8779	0.8094	0.8592	0.7193
ViT	0.9102	0.8296	0.9136	0.7870	0.9028	0.8141
SpectralFormer	0.9782	0.6700	0.9808	0.6770	0.9764	0.6431
SaaFormer	0.9837	0.9223	0.9821	0.9232	0.9824	0.9144

exhibit strong generalization capabilities and stability.

F. Visual Evaluation

We make a qualitative evaluation by visualizing the classification maps obtained by different methods. Figs. 8 and 9 provide the obtained results for Salinas dataset and Figs. 10 and 11 are the results for PaviaU dataset, respectively.

From the visualization of the datasets, it can be observed that our proposed SaaFormer obtains desirable classification maps. In the case of block-wise sampling and random sampling, especially in terms of texture and edge details. Furthermore, we selected a region of interest (ROI) zoomed in two times to highlight the differences in classification maps between different models, further evaluating classification performance more intuitively. As can be seen from these ROIs,

a remarkable phenomenon is that our model shows more realistic and finer details. Therefore, the visualization of the classification results clearly demonstrates that our proposed SaaFormer, incorporating both axial Transformer block and multi-level spectral extraction structure, achieves remarkably favorable classification maps in terms of texture and edge details.

IV. CONCLUSION

HSI are typically represented as a data cube with spatial-spectral information, which can be generally regarded as a sequence of data along the spectral dimension. Due to the difficulty of obtaining hyperspectral data and the limited data set, we find that there is a serious data leakage problem in the evaluation method of the existing HSI classification model.

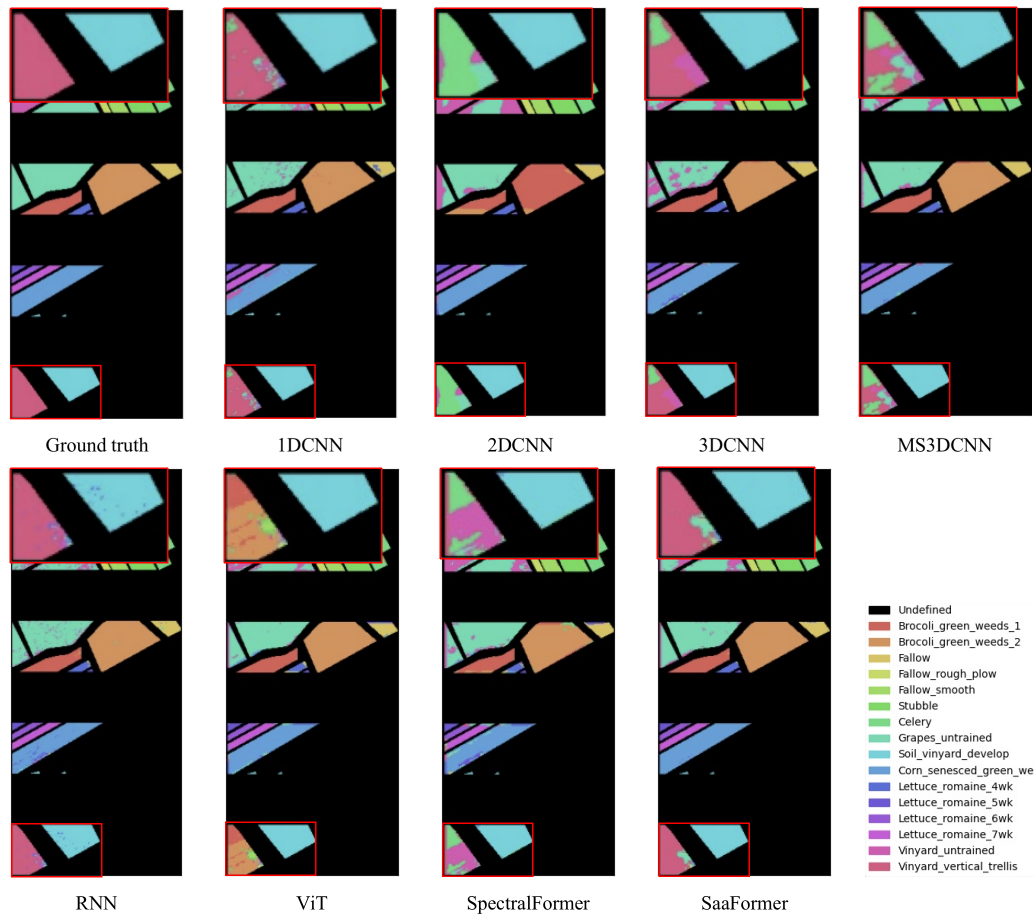


Fig. 8: Spatial distribution of testing sets using block-wise sampling, and the classification maps obtained by different models on the Salinas dataset

TABLE III: ABLATION ANALYSIS OF THE PROPOSED SaaFormer WITH A COMBINATION OF DIFFERENT STRUCTURE ON THE SIX DATASETS.

	Multi-level Spectral Extraction	Random Sampling			Block-wise Sampling		
		OA	AA	Kappa	OA	AA	Kappa
Botswana	✓	0.9837	0.9821	0.9824	0.9223	0.9232	0.9144
	×	0.9779	0.9804	0.9774	0.9041	0.9184	0.8947
KSC	✓	0.9676	0.9424	0.9640	0.8339	0.7740	0.8069
	×	0.9521	0.9339	0.9530	0.8276	0.7103	0.8031
IndianPines	✓	0.9727	0.9626	0.9683	0.8947	0.8713	0.8797
	×	0.9705	0.9612	0.9663	0.8807	0.8619	0.8698
PaviaU	✓	0.9875	0.9795	0.9833	0.9828	0.9649	0.9726
	×	0.9757	0.9772	0.9503	0.9824	0.9573	0.9720
PaviaC	✓	0.9944	0.9810	0.9921	0.9828	0.9649	0.9820
	×	0.9872	0.9776	0.9890	0.9765	0.9275	0.9649
Salinas	✓	0.9928	0.9967	0.9920	0.9253	0.9653	0.9163
	×	0.9559	0.9804	0.9510	0.9246	0.9637	0.9154

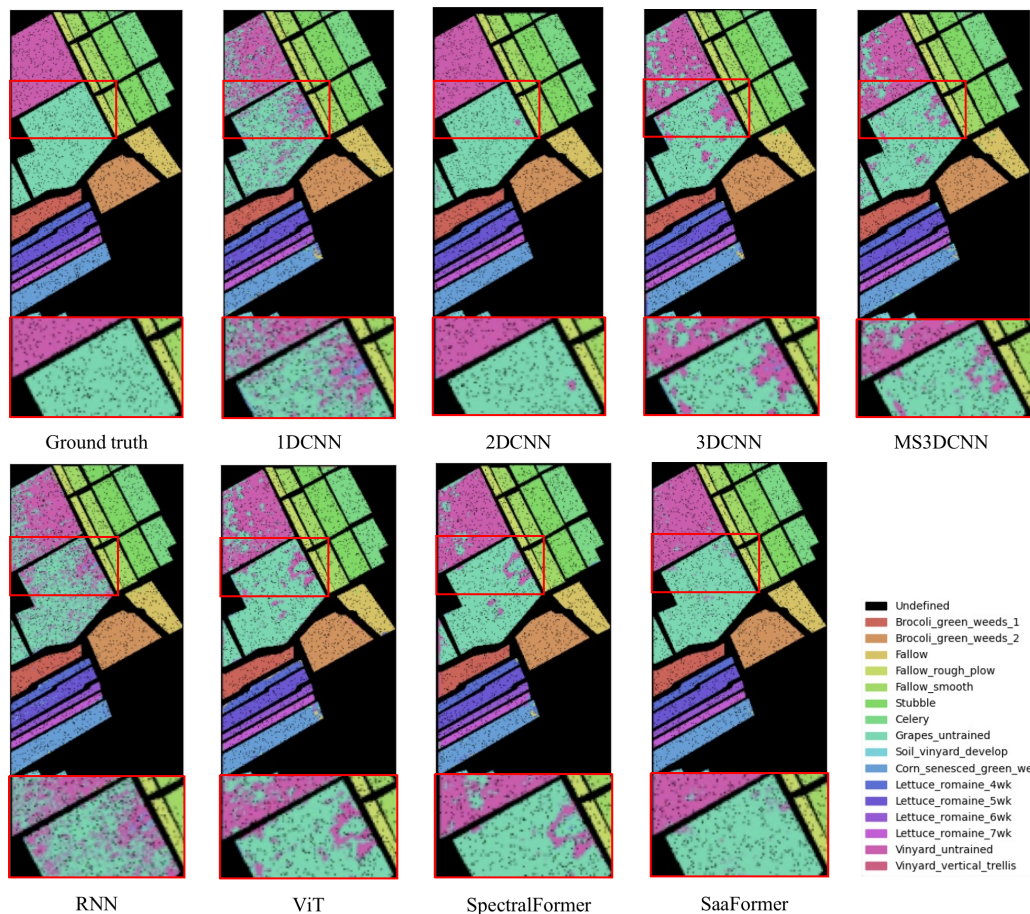


Fig. 9: Spatial distribution of testing sets using random sampling, and the classification maps obtained by different models on the Salinas dataset

This leads to an inaccurate evaluation of the generalization of the model, thus, we propose a block-wise sampling method to avoid data leakage at sample points while maintaining non-local training samples. Otherwise, different from CNNs that focus mainly on contextual information modeling, transformers have been proven to be a powerful architecture in characterizing the sequential properties globally. However, the classic ViT networks inevitably suffer from performance degradation when processing HS-like data. This might be explained well by the fact that ViT fails to model locally detailed spectral discrepancies. To this end, in this paper, we proposed a novel transformer-based model, named SaaFormer, which demonstrates robust generalization ability. And it comprises two primary components: axial aggregation attention and multi-level spectral extraction. The results on six publicly available datasets demonstrate that our model exhibits comparable performance when using random sampling, while significantly outperforming other methods when employing block-wise sampling partition.

REFERENCES

- [1] D. Hong et al., “Interpretable hyperspectral artificial intelligence: When nonconvex modeling meets hyperspectral remote sensing,” *IEEE Geosci. Remote Sens. Mag.*, vol. 9, no. 2, pp. 52–87, Jun. 2021.
- [2] M. Wang, Q. Wang, J. Chanussot, and D. Hong, “ $L_0 - L_1$ hybrid total variation regularization and its applications on hyperspectral image mixed noise removal and compressed sensing,” *IEEE Trans. Geosci. Remote Sens.*, vol. 59, no. 9, pp. 7695–7710, Sep. 2021, doi:10.1109/TGRS.2021.3055516.
- [3] J. Peng et al., “Low-rank and sparse representation for hyperspectral image processing: A review,” *IEEE Geosci. Remote Sens. Mag.*, early access, Jun. 10, 2021, doi: 10.1109/MGRS.2021.3075491.
- [4] F. Luo, T. Guo, Z. Lin, J. Ren, and X. Zhou, “Semisupervised hypergraph discriminant learning for dimensionality reduction of hyperspectral image,” *IEEE J. Sel. Topics Appl. Earth Observ. Remote Sens.*, vol. 13, pp. 4242–4256, 2020.
- [5] J. Yao, D. Meng, Q. Zhao, W. Cao, and Z. Xu, “Nonconvex-sparsity and nonlocal-smoothness-based blind hyperspectral unmixing,” *IEEE Trans. Image Process.*, vol. 28, no. 6, pp. 2991–3006, Jun. 2019.
- [6] Y. Yuan, Z. Zhang, and Q. Wang, “Improved collaborative non-negative matrix factorization and total variation for hyperspectral unmixing,” *IEEE J. Sel. Topics Appl. Earth Observ. Remote Sens.*, vol. 13, pp. 998–1010, 2020.
- [7] L. Gao, Z. Han, D. Hong, B. Zhang, and J. Chanussot, “CyCUnet: Cycle-consistency unmixing network by learning cascaded autoencoders,” *IEEE Trans. Geosci. Remote Sens.*, early access, Mar. 23, 2021, doi: 10.1109/TGRS.2021.3064958.
- [8] D. Hong et al., “Endmember-guided unmixing network (EGU-Net): A general deep learning framework for self-supervised hyperspectral unmixing,” *IEEE Trans. Neural Netw. Learn. Syst.*, early access, May 28, 2021, doi: 10.1109/TNNLS.2021.3082289.
- [9] J. Peng, W. Sun, and Q. Du, “Self-paced joint sparse representation for the classification of hyperspectral images,” *IEEE Trans. Geosci. Remote Sens.*, vol. 57, no. 2, pp. 1183–1194, Feb. 2019.
- [10] Q. Li, B. Zheng, B. Tu, J. Wang, and C. Zhou, “Ensemble EMDbased spectral-spatial feature extraction for hyperspectral image classification,”

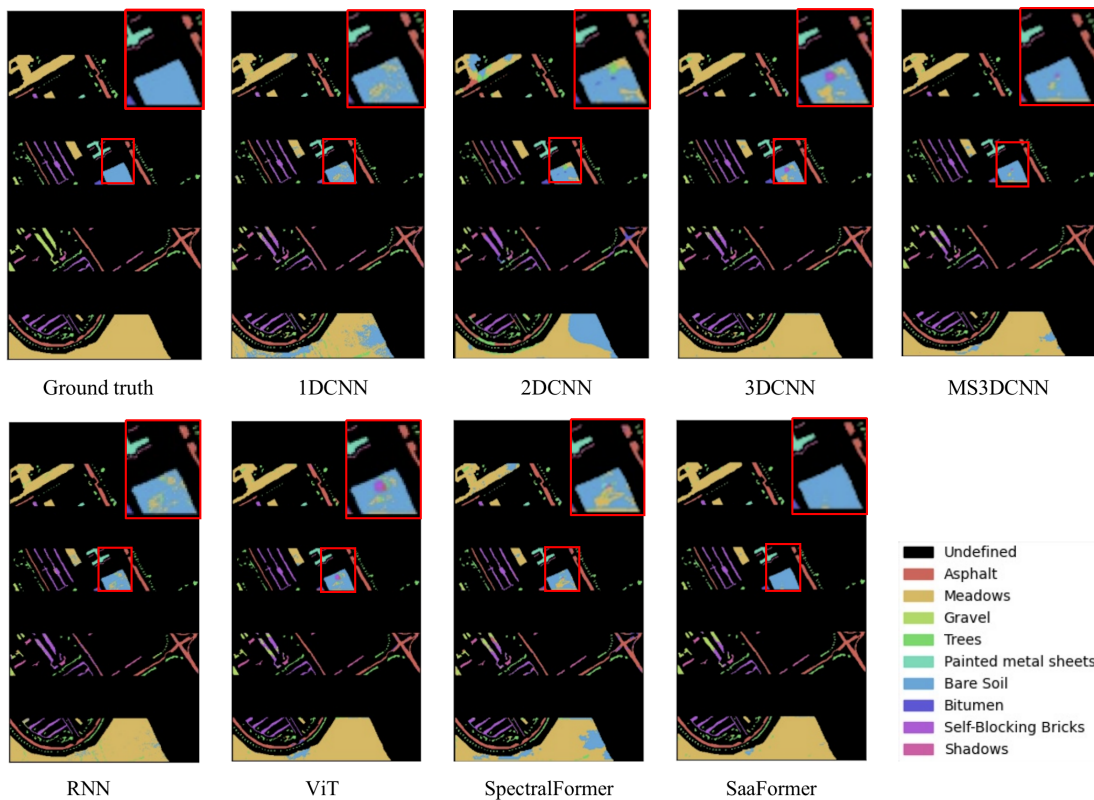


Fig. 10: Spatial distribution of testing sets using block-wise sampling, and the classification maps obtained by different models on the PaviaU dataset

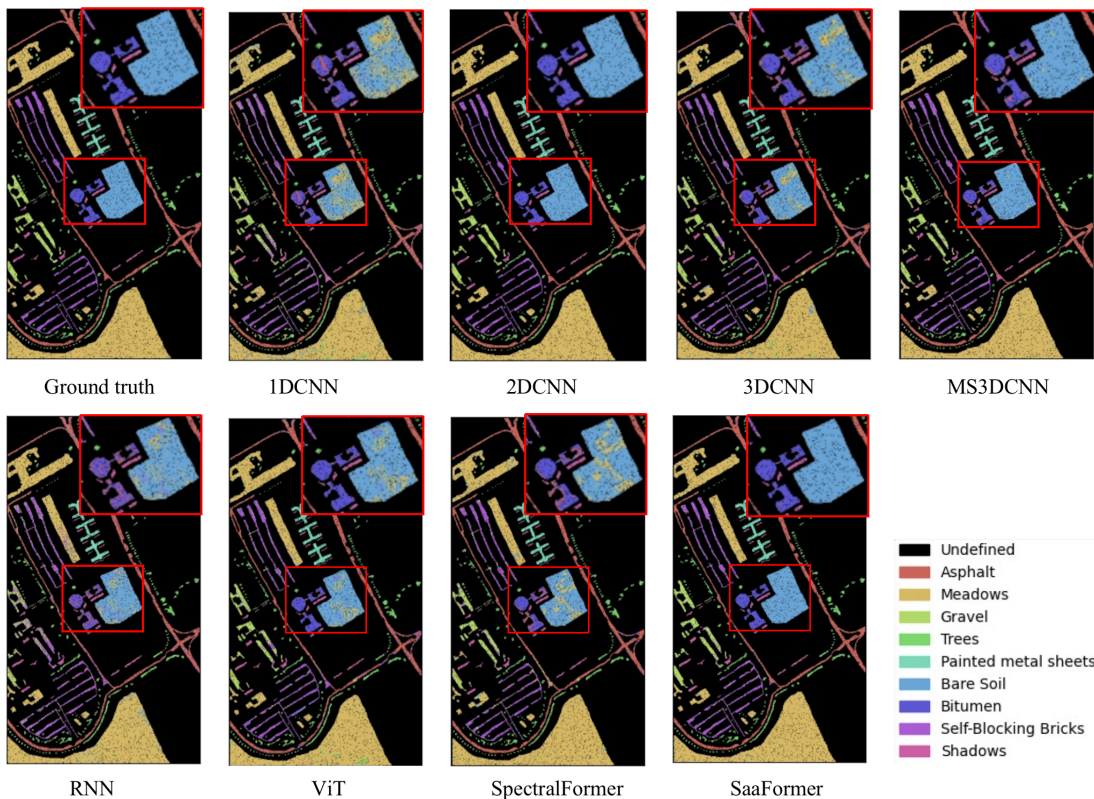


Fig. 11: Spatial distribution of testing sets using random sampling, and the classification maps obtained by different models on the PaviaU dataset

- IEEE J. Sel. Topics Appl. Earth Observ. Remote Sens., vol. 13, pp. 5134–5148, 2020.
- [11] Richards J A, Jia X, "Using suitable neighbors to augment the training set in hyperspectral maximum likelihood classification," *IEEE Geoscience and Remote Sensing Letters*, vol. 5, no. 4, pp. 774-777, 2008.
 - [12] Peng J, Li L, Tang Y Y, "Maximum likelihood estimation-based joint sparse representation for the classification of hyperspectral remote sensing images," *IEEE transactions on neural networks and learning systems*, vol. 30, no. 6, pp. 1790-1802, 2018.
 - [13] Kuching S, "The performance of maximum likelihood, spectral angle mapper, neural network and decision tree classifiers in hyperspectral image analysis," *Journal of Computer Science*, vol. 3, no. 6, pp. 419-423, 2007.
 - [14] Chakravarty S, Paikaray B K, Mishra R, et al., "Hyperspectral image classification using spectral angle mapper," 2021 IEEE International Women in Engineering (WIE) Conference on Electrical and Computer Engineering (WIECON-ECE). IEEE, pp. 87-90, 2021.
 - [15] F. Melgani and L. Bruzzone, "Classification of hyperspectral remote sensing images with support vector machines," *IEEE Transactions on Geoscience and Remote Sensing*, vol. 42, no. 8, pp. 1778–1790, Aug 2004.
 - [16] Qingwang Wang, Yanfeng Gu, and Devis Tuia, "Discriminative multiple kernel learning for hyperspectral image classification," *IEEE Transactions on Geoscience and Remote Sensing*, vol. 54, no. 7, pp. 3912–3927, 2016.
 - [17] Qi Cheng, P.K. Varshney, and M.K. Arora, "Logistic regression for feature selection and soft classification of remote sensing data," *IEEE Geoscience and Remote Sensing Letters*, vol. 3, no. 4, pp. 491–494, Oct 2006.
 - [18] M. Khodadadzadeh, Jun Li, A. Plaza, and J.M. Bioucas-Dias, "A subspace-based multinomial logistic regression for hyperspectral image classification," *IEEE Geoscience and Remote Sensing Letters*, vol. 11, no. 12, pp. 2105–2109, Dec 2014.
 - [19] Yoshua Bengio, Aaron Courville, and Pierre Vincent, "Representation learning: A review and new perspectives," *IEEE Transactions on Pattern Analysis and Machine Intelligence*, vol. 35, no. 8, pp. 1798–1828, 2013.
 - [20] Y. LeCun, Y. Bengio, and G. Hinton, "Deep learning," *Nature*, vol. 521, pp. 436–444, May 2015.
 - [21] Yushi Chen, Zhouhan Lin, Xing Zhao, Gang Wang, and Yanfeng Gu, "Deep learning-based classification of hyperspectral data," *IEEE Journal of Selected Topics in Applied Earth Observations and Remote Sensing*, vol. 7, no. 6, pp. 2094–2107, June 2014.
 - [22] Wei Hu, Yangyu Huang, Li Wei, Fan Zhang, and Hengchao Li, "Deep convolutional neural networks for hyperspectral image classification," *Journal of Sensors*, 501:258619, 2015.
 - [23] L. Mou, P. Ghamisi, and X. X. Zhu, "Deep recurrent neural networks for hyperspectral image classification," *IEEE Transactions on Geoscience and Remote Sensing*, vol. 55, no. 7, pp. 3639–3655, July 2017.
 - [24] Y. Yan, Y. Zhao, H.-f. Xue, X.-d. Kou, and Y. Liu, "Integration of spatial-spectral information for hyperspectral image classification," in 2010 Second IITA International Conference on Geoscience and Remote Sensing, pp. 242–245, Qingdao, 2010.
 - [25] X. Xu, J. Li, Y. Zhang, and S. Li, "A subpixel spatial-spectral feature mining for hyperspectral image classification," in IGARSS 2018 - 2018 IEEE International Geoscience and Remote Sensing Symposium, pp. 8476–8479, Valencia, Spain, 2018.
 - [26] Michael D Farrell and Russell M Mersereau, "On the impact of PCA dimension reduction for hyperspectral detection of difficult targets," *IEEE Geoscience and Remote Sensing Letters*, vol. 2, no. 2, pp. 192–195, 2005.
 - [27] Jun Yue, Wenzhi Zhao, Shanjun Mao, and Hui Liu, "Spectral-spatial classification of hyperspectral images using deep convolutional neural networks," *Remote Sensing Letters*, vol. 6, no. 6, pp. 468–477, 2015.
 - [28] Heming Liang and Qi Li, "Hyperspectral imagery classification using sparse representations of convolutional neural network features," *Remote Sensing*, vol. 8, no. 2, 2016.
 - [29] Y. Chen, H. Jiang, C. Li, X. Jia, and P. Ghamisi, "Deep feature extraction and classification of hyperspectral images based on convolutional neural networks," *IEEE Trans. Geosci. Remote Sens.*, vol. 54, no. 10, pp. 6232–6251, Oct. 2016.
 - [30] Li Y, Zhang H, Shen Q, "Spectral-spatial classification of hyperspectral imagery with 3D convolutional neural network," *Remote Sensing*, vol. 9, no. 1, pp. 67, 2017.
 - [31] M. He, B. Li and H. Chen, "Multi-scale 3D deep convolutional neural network for hyperspectral image classification," 2017 IEEE International Conference on Image Processing (ICIP), Beijing, China, 2017, pp. 3904-3908, doi: 10.1109/ICIP.2017.8297014.
 - [32] Dosovitskiy A, Beyer L, Kolesnikov A, et al., "An image is worth 16x16 words: Transformers for image recognition at scale," arXiv preprint arXiv:2010.11929, 2020.
 - [33] D. Hong et al., "SpectralFormer: Rethinking Hyperspectral Image Classification With Transformers," in *IEEE Transactions on Geoscience and Remote Sensing*, vol. 60, pp. 1-15, 2022, Art no. 5518615, doi: 10.1109/TGRS.2021.3130716.
 - [34] Shen, Zhuoran, et al., "Efficient attention: Attention with linear complexities." *Proceedings of the IEEE/CVF winter conference on applications of computer vision*. 2021.
 - [35] Liu, Ze, et al., "Swin transformer: Hierarchical vision transformer using shifted windows." *Proceedings of the IEEE/CVF international conference on computer vision*. 2021.
 - [36] Dong, Xiaoyi, et al., "Cswin transformer: A general vision transformer backbone with cross-shaped windows." *Proceedings of the IEEE/CVF Conference on Computer Vision and Pattern Recognition*. 2022.
 - [37] Han, Kai, et al., "Transformer in transformer." *Advances in Neural Information Processing Systems* 34 (2021): 15908-15919.
 - [38] Zhu, Chen, et al., "Long-short transformer: Efficient transformers for language and vision." *Advances in neural information processing systems* 34 (2021): 17723-17736.
 - [39] Huang, Zilong, et al., "Ccnet: Criss-cross attention for semantic segmentation." *Proceedings of the IEEE/CVF international conference on computer vision*. 2019.
 - [40] Jonathan Ho, Nal Kalchbrenner, Dirk Weissenborn, and Tim Salimans, "Axial attention in multidimensional transformers," arXiv preprint arXiv:1912.12180, 2019.
 - [41] Wang H, Zhu Y, Green B, et al., "Axial-deeplab: Stand-alone axial-attention for panoptic segmentation," *Computer Vision–ECCV 2020: 16th European Conference, Glasgow, UK, August 23–28, 2020, Proceedings, Part IV*. Cham: Springer International Publishing, 2020: 108-126.
 - [42] Valanarasu J M J, Oza P, Hacihaliloglu I, et al., "Medical transformer: Gated axial-attention for medical image segmentation," *Medical Image Computing and Computer Assisted Intervention–MICCAI 2021: 24th International Conference, Strasbourg, France, September 27–October 1, 2021, Proceedings, Part I* 24. Springer International Publishing, 2021: 36-46.
 - [43] Wan, Qiang, et al., "Seaformer: Squeeze-enhanced axial transformer for mobile semantic segmentation." arXiv preprint arXiv:2301.13156 (2023).
 - [44] Ramachandran, Prajit, et al., "Stand-alone self-attention in vision models." *Advances in neural information processing systems* 32 (2019).
 - [45] D. P. Kingma and J. Ba, "Adam: A method for stochastic optimization," 2014, arXiv:1412.6980.
 - [46] Nitish Srivastava, Geoffrey Hinton, Alex Krizhevsky, Ilya Sutskever, and Ruslan Salakhutdinov, "Dropout: a simple way to prevent neural networks from overfitting," *Journal of Machine Learning Research*, vol. 15, no. 1, pp. 1929–1958, 2014.